ACS Catalysis
Research Article
pubs.acs.org/acscatalysis

Nanocast $LaNiO_3$ Perovskites as Precursors for the Preparation of Coke-Resistant Dry Reforming Catalysts

Mahesh Muraleedharan Nair,[†] Serge Kaliaguine,*[,§] and Freddy Kleitz*[,†]

[†]Department of Chemistry and Centre de Recherche sur les Matériaux Avancés (CERMA), Université Laval, 1045 Avenue de la Médecine, Quebec City G1V 0A6, Canada

[§]Department of Chemical Engineering, Université Laval, 1065 Avenue de la Médecine, Quebec City G1V 0A6, Canada

S *Supporting Information*

ABSTRACT: Dry reforming of methane is gaining great interest owing to the fact that this process efficiently converts two greenhouse gases (CH_4 and CO_2) into synthesis gas ($CO + H_2$), which can be further processed into liquid fuels and chemicals. Herein, a perovskite-derived nanostructured Ni/La_2O_3 material is reported as an efficient and stable catalyst for this reaction. High-surface-area $LaNiO_3$ perovskite precursor is first synthesized by the method of nanocasting using ordered mesoporous silica SBA-15 as a hard template. The resulting nanostructured perovskite was found to possess high specific surface area as obtained from the BET method (150 $m^2\ g^{-1}$). The reduction behavior of the nanocast perovskite was monitored by performing the temperature-programmed reduction of hydrogen (TPR-H_2). It has been found that the complete destruction of perovskite structure occurs below 700 °C, leading to the formation of highly dispersed Ni^0 in La_2O_3, as observed in the XRD pattern of the material after reduction. Similar behavior was observed for the $LaNiO_3$ perovskite synthesized using the conventional citrate process. However, the specific surface area of the former material was found to be much higher than that of the latter (50 $m^2\ g^{-1}$), which obviously resulted from the mesoporous architecture of the nanocast $LaNiO_3$. It was found that the nanostructured Ni/La_2O_3 obtained from the reduction of the nanocast $LaNiO_3$ exhibited high activity for the conversion of the reactant gases (CH_4 and CO_2) compared to the catalyst obtained from conventional perovskite, under the reaction conditions used in the present study. Particularly, no coke formation was observed for the mesoporous catalyst under the present conditions of operation, which in turn reflects the enhanced stability of the catalyst obtained from the nanocast $LaNiO_3$. The improved performance of the nanostructured catalyst is attributed to the accessibility of the active sites resulting from the high specific surface area and the confinement effect leading to the stabilization of Ni nanoparticles.

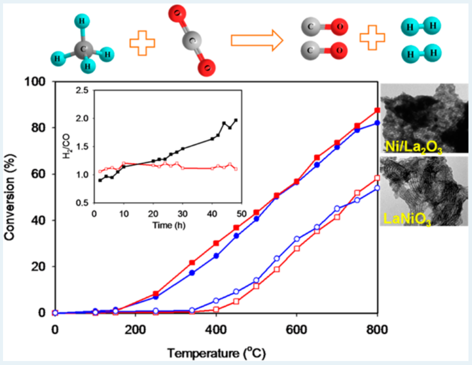

KEYWORDS: *dry reforming, nanocasting, perovskites, coke resistance, high surface area, synthesis gas, mesoporous*

1. INTRODUCTION

Clean and energy efficient technologies mostly rely on high temperature catalytic conversions, prominent examples being the hydrocarbon reforming reactions either in the presence of H_2O (steam reforming)[1−3] or in the presence of CO_2 (dry reforming).[4−6] Steam reforming (eq 1) is used commercially on a large scale as an effective method for producing hydrogen and synthesis gas ($CO + H_2$). Alternatively, dry reforming of methane (eq 2) is gaining attention because it consumes two greenhouse gases (CH_4 and CO_2) and converts them into synthesis gas, which can further be processed into liquid fuels or chemicals.

$$CH_4 + H_2O \rightarrow CO + 3H_2 \qquad \Delta H^0 = 206\ \text{kJ mol}^{-1} \qquad (1)$$

$$CH_4 + CO_2 \rightarrow 2CO + 2H_2 \qquad \Delta H^0 = 247\ \text{kJ mol}^{-1} \qquad (2)$$

Indeed, the produced synthesis gas (H_2/CO ratio close to unity) is highly desirable for the industrial production of many valuable chemicals.[7,8] The dry reforming reaction shows also great potential in energy transfer and storage systems due to its high endothermicity.[9]

Thus far, noble metals were found to be the most active catalysts for dry reforming.[10−13] However, previous studies showed that Ni metal could possibly replace the expensive noble metal catalysts.[14−18] However, these studies revealed that the major problem associated with Ni-based catalysts is that they also catalyze the formation of coke (carbon). Such carbon formation on the surface of the catalyst impedes the activity and thereby affects the long-term stability, which in turn hinders industrial applications of Ni catalysts. Various strategies were developed either to avoid or to minimize the coke deposition on the catalyst surface during dry reforming (e.g., reducing the particle size, use of a promoter, using a basic support, etc.).[19] Alternatively, resistance to coke formation can be significantly enhanced if the nickel catalyst is located within a well-defined

Received: June 27, 2014
Revised: September 6, 2014
Published: September 11, 2014

dx.doi.org/10.1021/cs500918c | *ACS Catal.* 2014, 4, 3837−3846

structure. For this, preformed crystalline oxides (such as spinels or perovskites) that contain the active metal homogeneously dispersed inside the bulk can be used as catalyst precursors.[20,21] Upon reduction, these oxides lead to the migration of some of the active metals to the surface, resulting in homogeneous distribution of active metal sites on the support. In this case, the metal−support interaction and hence the thermal stability can also be enhanced. A well-known example is the formation of Ni/La_2O_3 by performing the reduction of a $LaNiO_3$ perovskite precursor. Previous reports suggested that these materials are active for dry reforming.[21−25] However, multiple heat treatment steps involved in the synthesis of these materials generally results in the formation of catalysts with extremely low values of specific surface area. Therefore, efforts are still needed to produce such catalysts with high specific surface area and to substantiate the influence of Ni dispersion on the performance of these materials in the dry reforming reaction.

Nanocasting is a highly versatile method which enables the synthesis of various nonsiliceous mesoporous materials with extremely high values of specific surface area (oxides, carbon, etc.).[26,27] These nanostructured materials are found to be proficient for a multitude of applications such as catalysts, sensors, batteries, and so forth.[28−30] Recently, we reported the synthesis of high surface area perovskite-structured mixed metal oxides by using the nanocasting method.[31] These materials exhibited high catalytic activity for the total oxidation of methanol. Although the nanocasting method is widely preferred for the synthesis of a range of oxide and non-oxide compositions, these nanocast materials are still rarely used for applications involving high temperatures. Moreover, the high temperature structural modifications which can take place in the nanocast materials are rarely studied,[32] especially for mixed metal oxide compositions.

Here, we report on the synthesis of nanocast mesoporous $LaNiO_3$, prepared using ordered mesoporous SBA-15 silica as the hard template (Supporting Information, Figure S1), and the resulting nanostructured Ni/La_2O_3 catalyst obtained by postsynthesis reduction of the nanocast perovskite. Furthermore, the activity and stability of the high surface area materials in catalytic dry reforming of methane are demonstrated. Comparisons were made using Ni/La_2O_3 obtained from conventional bulk $LaNiO_3$ perovskite synthesized using the citrate method. Our work shows that the materials obtained by nanocasting are greatly superior to those of similar composition obtained from the conventional process. Moreover, exceptional resistance of the nanocast materials to coke formation is revealed, which is particularly significant for catalytic applications.

2. EXPERIMENTAL SECTION

2.1. Synthesis of Ordered Mesoporous SBA-15. SBA-15 was synthesized using pluronic P123 as the structure directing agent and tetraethylorthosilicate (TEOS) as the silicon source.[33,34] In a typical synthesis, 4 g of P123 was dissolved in 76 g of deionized water and 4.3 g of hydrochloric acid (37%) at 35 °C under magnetic stirring. To the obtained homogeneous solution, 8.6 g of TEOS was rapidly added with continued stirring for 24 h at 35 °C and subsequently subjected to hydrothermal treatment at 100 °C for an additional 24 h, to ensure further framework condensation. After cooling, the resulting solution was filtered, and the solid product was dried at 100 °C for 24 h. Finally, the powder was calcined at 550 °C in order to remove the organic copolymer template.

2.2. Synthesis of $LaNiO_3$ Precursors. Nanocasting was performed using a citrate complex of lanthanum and nickel as the precursor for perovskite.[31] In a typical synthesis, 3 mmol each of $La(NO_3)_3{\cdot}6H_2O$ and $Ni(NO_3)_3{\cdot}6H_2O$ were dissolved in an ethanolic solution of citric acid (10 mL) to obtain an equimolar solution, which was then added slowly to 1 g of SBA-15 dispersed in 10 mL of distilled water. The mixture was stirred for 4 h at room temperature, and subsequently, the solvent was evaporated under vacuum using a rotary evaporator. The thus-obtained powder was further dried at 80 °C for 24 h, ground well in a mortar, and calcined at 500 °C for 4 h at the rate of 2 °C min^{-1} with an intermediate dwell at 170 °C for 2 h. The molar ratio of metal ions to citric acid was kept at 2:1. Impregnation was repeated once for achieving higher loading. The final powder was calcined at 700 °C for 6 h with the same heating ramp as mentioned before. Finally, the silica template was removed by treating the composite three times with 2 M NaOH at room temperature. The final $LaNiO_3$ product (designated as LN-NC hereafter) was washed with water and ethanol and dried overnight at 80 °C.

For the synthesis of bulk perovskites,[25] 10 mmol each of $La(NO_3)_3{\cdot}6H_2O$ and $Ni(NO_3)_3{\cdot}6H_2O$ were dissolved in an aqueous solution of citric acid (10 mL). The mixture was stirred overnight at room temperature, and then the solvent was evaporated at 80 °C. The $LaNiO_3$ powder thus-obtained (designated as LN-C hereafter) was ground carefully in a mortar and calcined at 700 °C for 6 h.

For obtaining Ni/La_2O_3, both mesoporous and bulk perovskites were reduced at 700 °C for 2 h under a flow of 5% H_2 in argon. These materials are designated as LN-CR and LN-NCR to represent bulk or nanocast Ni/La_2O_3, respectively.

2.3. Characterization. Wide-angle powder XRD analysis was performed with a Siemens 80 Model D5000 diffractometer using Cu Kα radiation (λ = 0.15496 nm). N_2 physisorption analyses were performed at −196 °C with an ASAP 2010 sorption analyzer. Prior to analysis, samples were degassed overnight at 150 °C. Specific surface areas of nanocast perovskites were determined using the BET method on the lower relative pressure region of the adsorption isotherm (0.05−0.2). Pore size distributions were obtained by using the nonlocal density functional theory (NLDFT) method[34,35] assuming cylindrical pore geometry (applying the kernel of metastable NLDFT adsorption of N_2 in cylindrical pores on an oxide surface, i.e., adsorption branch) supplied by the Autosorb-1 1.55 software from Quantachrome Instruments. The total pore volume was calculated from the nitrogen sorption capacity at P/P_0 = 0.95. For TEM images, the samples were first dispersed in ethanol and deposited on carbon grids and analyzed on a JEOL JEM 1230 microscope. Scanning electron microscopy (SEM) images were obtained with a FEI Magellan 400 at a low landing energy (1.0 kV), without metal coating (KAIST, Daejeon, Republic of Korea).

X-ray photoelectron spectroscopy (XPS) spectra were collected on a Kratos Axis-Ultra electron spectrometer (U.K.) using a monochromatic Al Kα X-ray source at a power of 300 W and operated with a base pressure of 6.66×10^{-8} Pa (5×10^{-10} Torr). Charge compensation was required using a low-energy electron beam perpendicular to the surface of the samples. Survey spectra used for determining the elemental composition were collected at a pass energy of 160 eV and a step size of 1 eV. Ni is usually quantified with Ni(2p) or with

Ni(3s). However, in the present case, strong interferences were observed in Ni(2p) and Ni(3s) with La(3d) and La(4d), respectively. The interference free Ni(3p) signal is used in the present study. TPR-H_2 analysis was performed using an RXM-100 multicatalyst testing and characterization system. The catalyst (60 mg) was placed in a quartz reactor, which was pretreated under a flow of 20 mL min^{-1} (20% O_2 in He) at 500 °C for 1 h. The TPR was performed under a flow of 10 mL min^{-1} (5% H_2 in Ar) with a temperature ramp of 5 °C min^{-1} from 25 to 900 °C. The consumption of hydrogen was monitored with a thermal conductivity detector (TCD) and quantified.

2.4. Catalytic Tests. The catalytic activity of the materials was tested under steady state conditions. One hundred milligrams of the catalyst was inserted between two quartz wool plugs placed in a U-shaped quartz reactor (internal diameter = 5 mm). The temperature was controlled using a K-type thermocouple placed in the reactor without direct contact with the catalyst. To purge the catalytic system, the catalysts were first flushed with Ar for 1 h at room temperature. The feed, composed of CH_4 (10 mL min^{-1}), CO_2 (10 mL min^{-1}), and Ar as diluent with a total flow of 50 mL min^{-1} (GHSV = 2.1×10^5 h^{-1}) was passed through the reactor and the temperature was increased. Gas samples were collected in the steady-state regime at an interval of 2 h of constant conversion, and the products were analyzed with a gas chromatograph (HP 6890 series) equipped with a TCD. Reactants and products were separated with a Haye-Sep T column (internal diameter = 1 mm, L = 2 m × 5 m). Stability tests were performed at 700 °C for 48 h with all other conditions remaining the same.

The used catalyst was purged with He for 1 h and then treated at 800 °C in a flow of 5% O_2 in He. The CO_2 evolved was monitored using a gas chromatograph as a method to estimate the amount of residual carbon. Thermogravimetric analyses (TGA) of the used catalysts were performed using a NETZSCH STA 449C thermogravimetric analyzer under an air flow of 20 mL min^{-1} with a heating rate of 10 °C min^{-1}. The Raman spectra were recorded at 22.0 ± 0.5 °C using a LABRAM 800HR Raman spectrometer (Horiba Jobin Yvon, Villeneuve d'Ascq, France) coupled to an Olympus BX 30 fixed stage microscope. A 514.5 nm line of an Ar laser (Coherent, INNOVA 70C Series Ion Laser, Santa Clara, CA) was used as the excitation light source. The laser beam was focused on the sample at an intensity of approximately 5 mW.

3. RESULTS AND DISCUSSION

First, wide-angle X-ray diffraction analysis was performed to confirm the formation of the perovskite structure. The XRD patterns obtained for the synthesized perovskites (i.e., LN-NC and LN-C samples) are shown in Figure 1. As observed, both the nanocast and the bulk perovskites exhibit reflections characteristic of the single-phase orthorhombic $LaNiO_3$ structure. No peaks representing possible impurity (e.g., nickel or lanthanum oxide phases) were observed. For both LN-C and LN-NC, diffraction peaks were observed in the same regions; however, they had different intensities. The wide-angle XRD patterns of the perovskites after performing reduction at 700 °C for 2 h (Figure 1, blue and black curves) show that the perovskite structure is completely destroyed for both the nanocast and bulk $LaNiO_3$. All the observed peaks can be indexed either to La_2O_3 or to Ni^0. The sizes of the Ni particles were estimated from the X-ray line broadening by applying the Scherrer equation (see Table 1). Obviously, much smaller sized Ni particles dispersed on La_2O_3 were obtained when performing reduction of the nanocast mesoporous $LaNiO_3$ compared to its bulk counterpart.

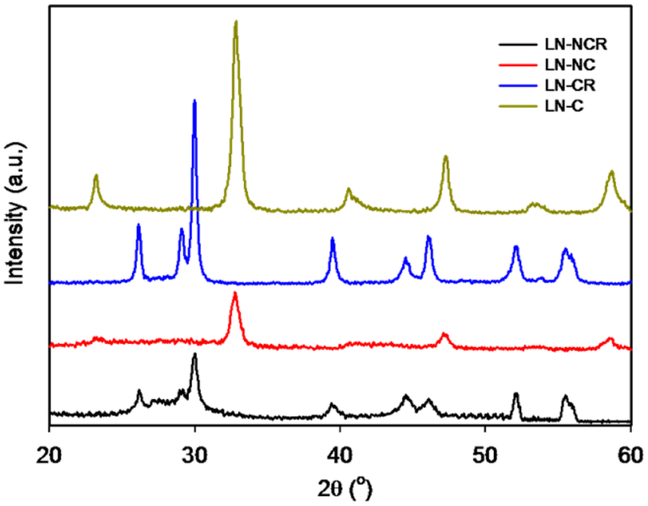

Figure 1. Wide-angle XRD patterns of $LaNiO_3$ and Ni/La_2O_3 (after reduction at 700 °C), as indicated.

Table 1. Structural Parameters of $LaNiO_3$ Perovskites and Ni/La_2O_3 Materials Obtained by Performing Reduction at 700 °C

sample	S_{BET}[a] (m^2g^{-1})	D_p[b] (nm)	Vp[c] (cm^3g^{-1})	Ni_{XRD}[d] (nm)
LN-C	10			
LN-CR	18			21
LN-NC	150	5.8	0.2	
LN-NCR	50	6.5	0.1	11

[a] Specific BET surface area. [b] NLDFT average pore size. [c] Total pore volume. [d] Ni particle size calculated by the Scherrer method.

Information regarding the formation of the mesostructure of nanocast $LaNiO_3$ was obtained by transmission electron microscopy (TEM). Representative images of all the samples are given in Figure 2. Ordered domains were observed along with the presence of fractions of disordered regions in the case of LN-NC. The nanoporous structure of the $LaNiO_3$ nanocast was also confirmed by high-resolution SEM analysis (Figure 3). The images indicate that, although the material appears rather disordered, its pore structure is quite open and accessible from the outside surface of the particles. The microscopy data are in line with the absence of sharp low-angle diffraction peaks in the XRD pattern of $LaNiO_3$ (data not shown).

After performing reduction treatment of nanocast $LaNiO_3$ at 700 °C, porosity was still persistent but to a lower extent, as evident from Figure 2g,h. For LN-C, large agglomerates constituting particles in the size range 50−100 nm were observed. This agglomeration resulted from sintering occurring at the high temperature necessarily used for the synthesis of these materials. Generally, high-temperature reduction of perovskites leads to the formation of nanoparticles of B site metal (e.g., Ni) dispersed on the oxide formed by the A site metal (e.g., La).[21−25] Here, the results obtained from wide-angle XRD analysis (Figure 1) clearly show diffraction peaks corresponding to Ni^0 and La_2O_3, without the presence of any impurity phase. Even though particle agglomeration still persists after reduction, it has been found that the extent of

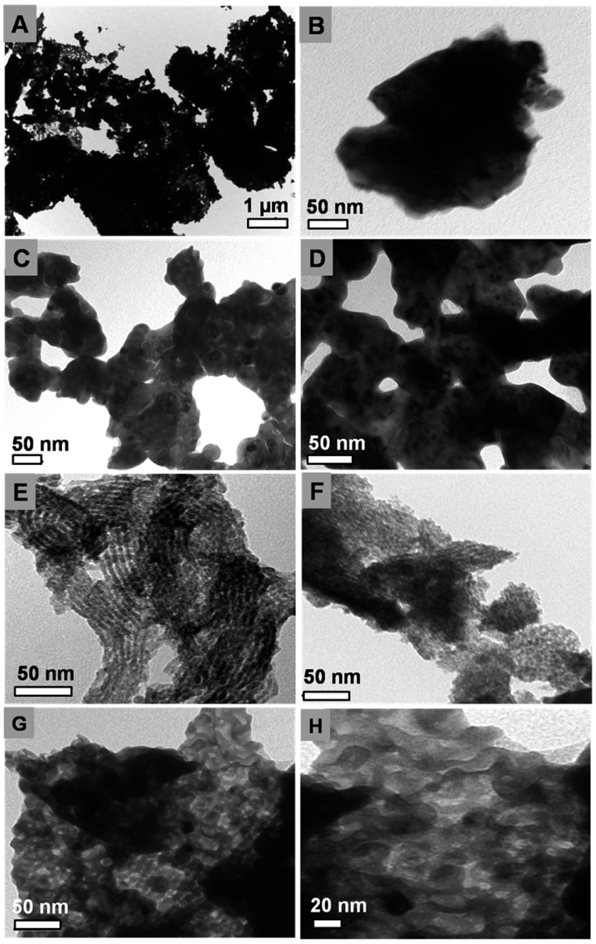

Figure 2. TEM images of LN-C (A, B), LN-CR (C, D), LN-NC (E, F), and LN-NCR (G, H).

agglomeration seems to be much lower compared to the parent perovskite, which might have resulted from the structural changes occurring during reduction (evidenced from XRD). The particle sizes of Ni estimated from the TEM images were found to vary between 5 and 20 nm, with the larger fraction centered approximately around 20 nm in agreement with the XRD results (Table 1).

Further, N_2 physisorption analysis was performed at −196 °C on both mesoporous and conventional $LaNiO_3$ perovskites and Ni/La_2O_3 obtained after the postsynthetic reduction treatment at 700 °C. The adsorption−desorption isotherms and corresponding pore size distributions are given in Figure 4.

The isotherm obtained for the nanocast $LaNiO_3$ exhibits type IV behavior, with a well-developed hysteresis loop appearing in the relative pressure range from 0.4 to 0.7. This observation agrees with previous reports on nanocast transition metal oxides.[28−31] Also, a small hysteresis loop was observed in the high relative pressure region, indicating the presence of interparticle pores.[36] A similar isotherm was observed in the case of Ni/La_2O_3 obtained from the reduction of nanocast $LaNiO_3$. However, the hysteresis loop becomes smaller in the latter case. Also, the volume adsorbed was found to be lower for the reduced material. All these observations indicate that a significant percentage of porosity was lost for the nanocast material after postsynthesis reduction at 700 °C. For $LaNiO_3$ synthesized using the conventional citrate process, the isotherm was found to match well with those generally observed for non porous bulk materials. In this case, the shape of the isotherm remains roughly the same after performing reduction treatment, with an enlargement of the hysteresis loop in the higher relative pressure region (Figure 4).

As reported in Table 1, the specific BET surface area of the nanocast $LaNiO_3$ was exceptionally high (150 $m^2\ g^{-1}$) compared to that obtained for the conventional $LaNiO_3$ (10 $m^2\ g^{-1}$), especially considering the high calcination temperature of 700 °C. Interestingly, this enhancement in the specific surface area persists in the case of nanocast material (50 $m^2\ g^{-1}$) in comparison to the bulk perovskite, even after performing the postsynthesis reduction treatment at 700 °C. Here, it is to be noted that the reduction treatment is performed after the removal of the silica template, and it is thus different from the initial calcination step. The pore sizes of the materials were derived from the adsorption branch by applying the NLDFT method.[34,35] The pore size distributions are found to be narrow for both as-synthesized and postreduced nanocast materials. The pore size of the nanocast materials was found to increase slightly after reduction (Table 1). Also, it has been found that the total pore volume of the bulk perovskite, even though very low, increased slightly after performing the reduction treatment at 700 °C. This implies that the collapse of the perovskite structure, leading to the formation of Ni/La_2O_3, resulted in the introduction of porosity to some extent, which also explains the slight enhancement of specific surface area of this bulk perovskite after reduction.

XPS analysis was performed for the nanocast $LaNiO_3$ and its derived Ni/La_2O_3 sample. For both these samples, strong interferences between Ni (2p) and La (3d) and Ni (3s) and La (4d) were observed. Hence, the interference-free Ni (3p) signal was used for the analysis of the surface Ni species (Supporting Information, Figure S2). For the nanocast $LaNiO_3$, a single

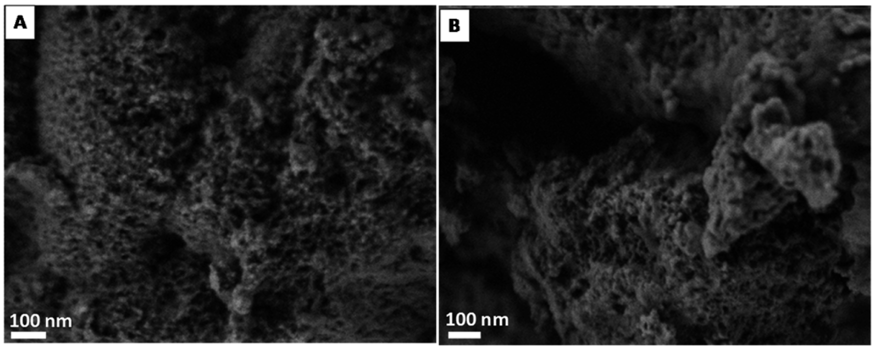

Figure 3. High-resolution SEM images of the nanocast $LaNiO_3$ perovskite sample (LN-NC) (A and B are different views).

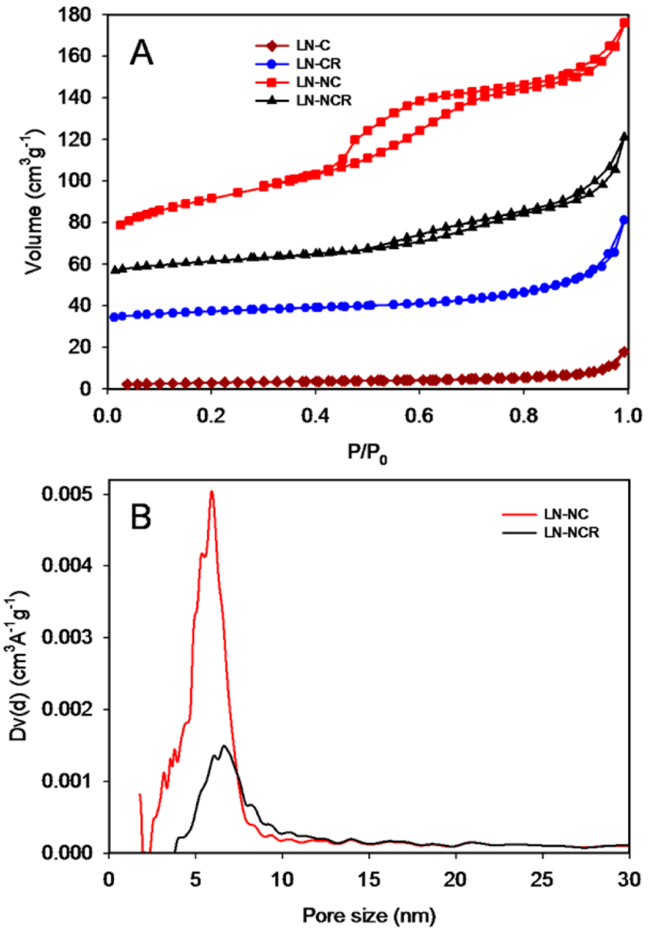

Figure 4. (A) N_2 physisorption isotherms of as-synthesized and reduced forms of nanocast and bulk $LaNiO_3$ perovskites. (B) NLDFT pore size distributions (adsorption branch) for as-synthesized and reduced nanocast $LaNiO_3$ as indicated (offsets: LN-CR, +30 $cm^3\ g^{-1}$; LN-NC, +50 $cm^3\ g^{-1}$; and LN-NCR, +50 $cm^3\ g^{-1}$).

peak centered at 65.9 eV was observed. This indicates that all the Ni species present at the surface are included in the perovskite structure. After reduction, it was found that the peak maxima shifted toward lower binding energy (64.9 eV), which is due to the fact that reduction of the perovskite structure occurred, leading to a change of chemical state of surface Ni species. In addition, a significant decrease in Ni/La atomic ratio was observed after the reduction treatment (0.30) in comparison to $LaNiO_3$ (1.68). These results point to the formation of small Ni particles situated most likely inside the pores of the La_2O_3 support.

In order to obtain information about the reduction behavior of as-synthesized perovskites, temperature-programmed reduction (TPR-H_2) treatment was performed. In general, the observed H_2 consumption peaks in the case of perovskites arise from the reduction of B site metal cation in the ABO_3 structure. The reduction profiles obtained are shown in Figure 5. Typically, two main reduction steps, one at low temperature and one at high temperature, were observed for the bulk $LaNiO_3$, which is in line with previous reports.[37,38] The first peak centered around 370 °C could be attributed to the reduction of Ni^{3+} in the perovskite structure to Ni^{2+}, leading to the formation of $La_2Ni_2O_5$. The shoulder visible around 390 °C for LN-C indicates further reduction of some nickel in the grain boundaries, as observed previously for $LaCoO_3$ synthesized by reactive grinding.[39] In the case of nanocast $LaNiO_3$, the reduction profile appears in a similar way, however, with the absence of the shoulder. This may correspond to the absence of grain boundaries in the nanocast materials. Also, from the peak position of the second reduction step, it can be implied that the complete reduction of the nanocast perovskite took place at a slightly lower temperature in comparison with the one prepared by the citrate method. The values of hydrogen consumption were determined for the nanocast and the bulk $LaNiO_3$ materials (Table 2). In general, the ratio of peak area of the second peak to that of the first being equal to 2 indicates that the first step of reduction corresponds to the formation of Ni^{2+}, which in turn gets reduced to Ni^0. For both LN-C and LN-NC, the values of hydrogen consumed during each step correspond perfectly with the formation of Ni^{2+} and Ni^0 during the respective stages of reduction.

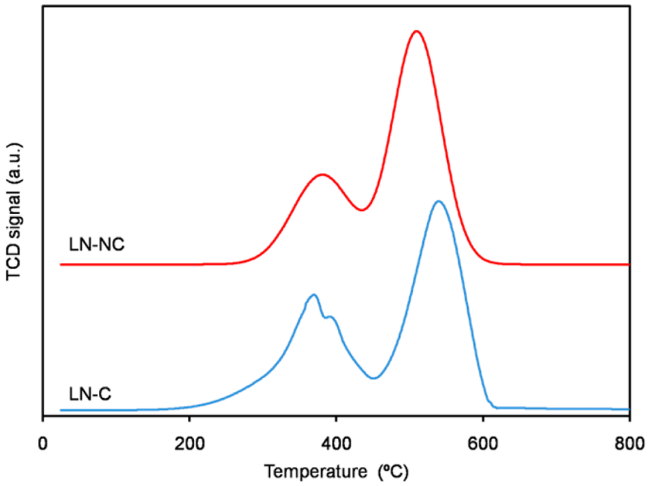

Figure 5. TPR-H_2 profiles of nanocast and bulk $LaNiO_3$ perovskites.

Table 2. Amount of H_2 Consumed during TPR-H_2

sample	first step ($mol_{H2}\ Ni^{-1}$)	second step ($mol_{H2}\ Ni^{-1}$)
LN-C	0.511	1.03
LN-NC	0.525	1.09

Initial monitoring of the catalytic activity was performed using as-synthesized perovskites without any reduction step. The conversion profiles for CH_4 and CO_2 obtained as a function of temperature are shown in Figure 6. It is well-known that the reduction of perovskite will take place under the conditions used for dry reforming, although higher temperatures are required for complete reduction compared to that necessary in the presence of H_2.[40] We found that in the case of LN-C, very low values of conversions were observed for both CH_4 and CO_2 until 800 °C. For LN-NC, comparatively higher conversions (approximately 40%) were observed under the same conditions. Incomplete reduction of the perovskite structure under the present reaction conditions could be the reason for the observed rather low values of conversion. In turn, this could lead to the lower exposure of the active Ni^0 phase to the reactants.

Figure 7 depicts the temperature-dependent conversion profiles for the bulk and nanocast catalysts, after performing the postreduction step. In this case, we observed almost 90% conversion for both CH_4 and CO_2 when LN-NCR was used as the catalyst, at 800 °C. In comparison, when LN-C was used

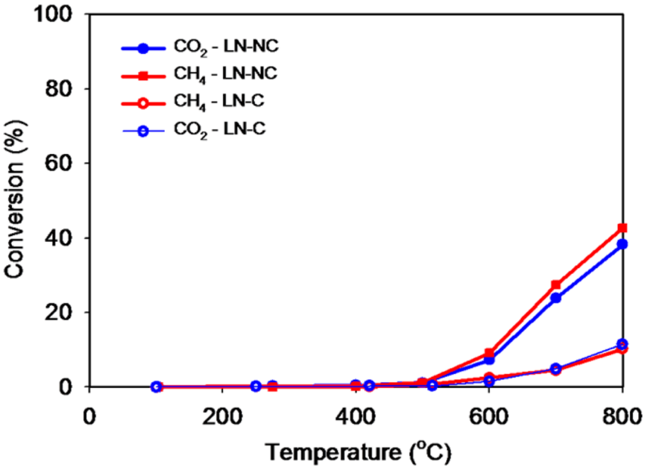

Figure 6. Temperature-dependent conversion profiles of CH_4 and CO_2 over nanocast and bulk $LaNiO_3$ perovskites (GHSV = 2.1 × 10^5 h^{-1}).

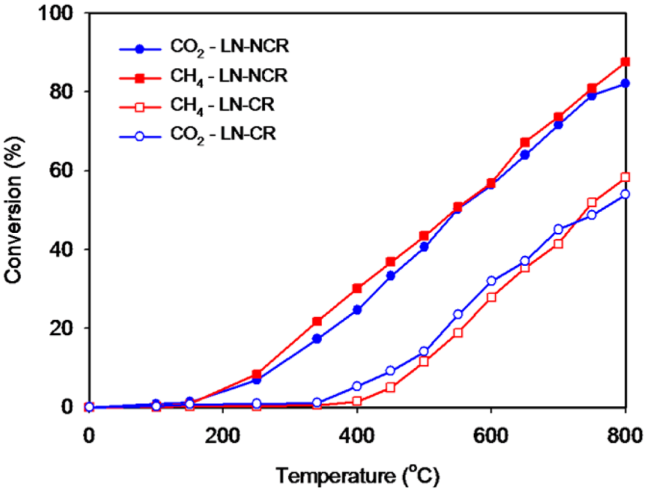

Figure 7. Temperature-dependent conversion profiles of CH_4 and CO_2 over Ni/La $_2O_3$ catalysts derived from nanocast and bulk $LaNiO_3$ perovskites (GHSV = 2.1 × 10 ^{5} h^{-1}).

after reduction, the values of conversion were found to be still less than 60%. Thus, it is clear that the performance of the LN-NCR catalyst obtained from nanocast $LaNiO_3$ is exceedingly better than that of LN-CR obtained from $LaNiO_3$ synthesized using the citrate process. Moreover, for the nanocast catalyst, the H_2/CO ratio remained closer to unity compared to what is observed for the citrate counterpart (Supporting Information, Figure S3).

Generally, the H_2/CO ratio is expected to be slightly lower than the stoichiometric value of one because the H_2 produced is partly consumed by the reverse water gas shift reaction (RWGS) (eq 3) during the dry reforming of methane.[41]

$$CO_2 + H_2 \rightarrow CO + H_2O \quad (3)$$

However, under the present reaction conditions, the product ratio was always found to be slightly above unity, which indicates the suppression of RWGS when Ni/La_2O_3 derived from nanocast mesoporous $LaNiO_3$ was used as the catalyst. A slight increase in the ratio with the increase in temperature, indicative of an increased selectivity toward hydrogen, was observed for the nanocast catalysts. This may be due to the fact that at higher temperatures the rate of methane decomposition is increased. Indeed for the entire temperature range studied, methane conversion was found to be slightly higher than CO_2 conversion. In the case of bulk LN-CR, the H_2/CO ratio was found to be highly dependent on the reactant temperature (Supporting Information, Figure. S3). In this case, because this ratio remains lower than one, RWGS seems to operate, especially at lower temperatures. Also, the CH_4 conversion was found to be slightly lower than that of CO_2 at lower temperatures until 750 °C, where it got reversed. At higher temperature, the H_2/CO ratio almost reached one.

A major concern in the development of Ni-based catalysts for dry reforming is their lack of durability, which is caused both by sintering and carbon deposition on the surface. Our initial experiments demonstrated that nanocast materials, either postreduced or not, are clearly efficient for the conversion of CO_2 and CH_4 in comparison to their bulk counterparts. Our results also indicate that Ni/La_2O_3 obtained by performing a reduction treatment exhibits greatly enhanced catalytic activity. These materials were thus analyzed to verify their long-term stability under reforming conditions. For this, after the reduction step, the catalyst was exposed to the flow of the reactant gases (CH_4 and CO_2) at 700 °C. In this experiment, constant values of conversions were observed for both CH_4 and CO_2 during the entire evaluation period, as shown in Figure 8a. For the catalysts derived from bulk $LaNiO_3$, constant conversions were observed during the first few hours. However, after 20 h, CO_2 conversion started to decline while CH_4 conversion almost remained constant. It then declined also after 40 h. The outlet products were analyzed at regular intervals continuously over 48 h. The experimental H_2/CO ratio obtained for nanocast Ni/La_2O_3 during this long-term run was found to remain constant near unity (Figure 8b). Note that the ratio remained slightly above one indicating the absence of RWGS during the entire period of the present investigation. For the catalysts synthesized using the citrate process, the H_2/CO ratio only remained close to and slightly above one during the initial hours of investigation. Then, a steady increase in the H_2/CO ratio was observed with respect to the exposure time, so that after 48 h this ratio reached 2.

After monitoring the conversions, the catalyst was purged with He for 1 h and then treated at 800 °C in a flow of 5% O_2 in He. The amount of carbon was determined from the amount of CO_2 evolved. Estimate of the amount of carbon deposited on the surface of the catalyst showed that initially both the catalysts obtained either by the citrate process or by nanocasting were found to be highly coke-resistant for short-term runs. No detectable amount of carbon was found on both catalysts after a single run. But most importantly, for the catalyst derived from nanocast $LaNiO_3$, no detectable amount of carbon was found after prolonged exposure to the reactant gases even after 48 h at 700 °C. This is in line with the fact that the extent of conversion remained constant throughout the period, and no noticeable variation was found on the H_2/CO ratio. On the other hand, for the citrate-based catalyst, it has been found that 16% carbon formed on the catalyst surface after a 48 h run, which would obviously be the reason for the decline of activity and the increase in the H_2/CO ratio with respect to time.

Deviations from thermodynamic predictions were observed in the case of conversions over the nanocast catalyst. Such deviations were previously documented in other cases, as discussed by various authors.[42−46] Also, the values of

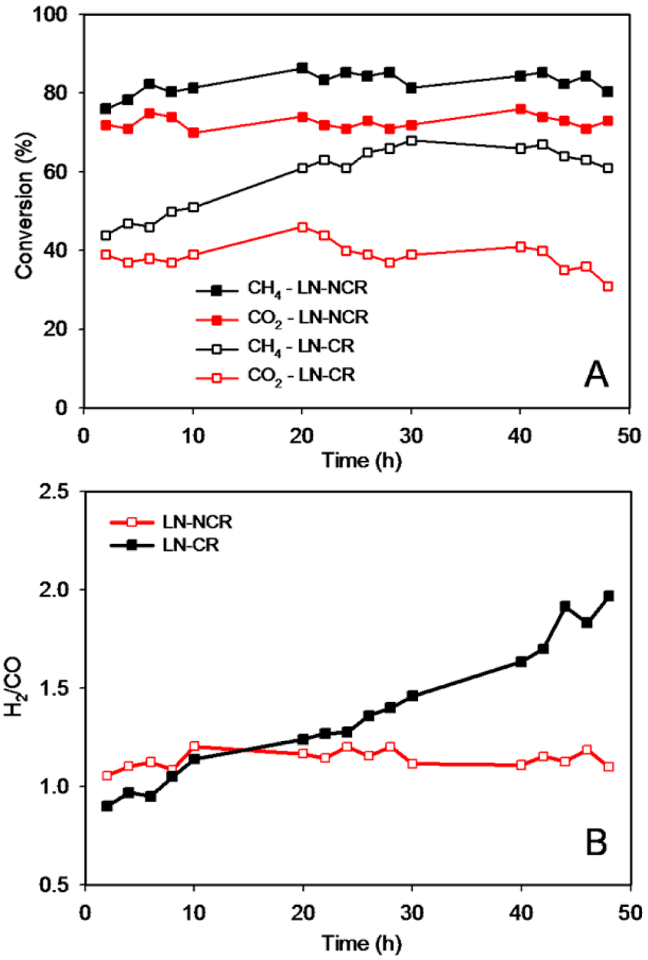

Figure 8. (A) CH_4 and CO_2 conversions as a function of time on stream at 700 °C over Ni/La_2O_3 catalysts derived from nanocast and bulk $LaNiO_3$ (GHSV = 2.1×10^5 h^{-1}). (B) Variation of experimental ratios vs time on stream at 700 °C over Ni/La_2O_3 catalysts derived from nanocast and bulk $LaNiO_3$ perovskites (GHSV = 2.1×10^5 h^{-1}).

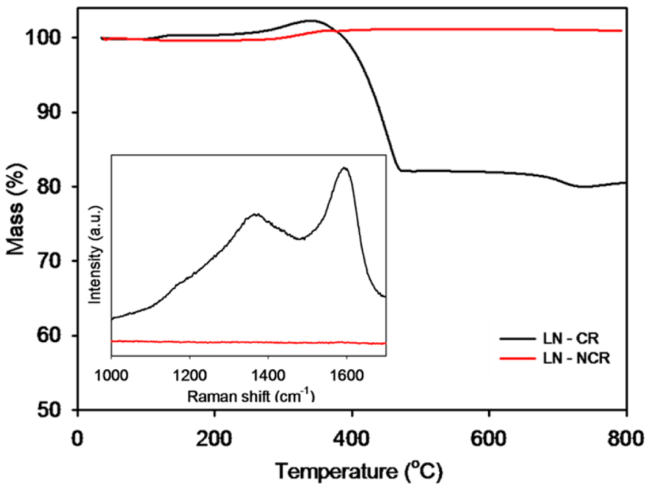

Figure 9. Thermogravimetric analysis of the catalysts after stability tests for 48 h (inset: Raman spectra of the two used catalysts).

conversion observed in the case of the nanocast catalyst in the present study are in agreement with what was reported previously for other catalysts.[16,47,48] In addition, we note that the values of H_2/CO are found to be slightly higher than unity, which could possibly be caused by some minor carbon deposition on the catalyst surface. However, we could not observe the presence of any noticeable amount of carbon after 48 h of exposure to the reaction conditions. Such variations in the product ratios were also reported by other authors without the deposition of carbon on the surface.[16,47,49,50] A possible hypothesis for such a discrepancy could be the formation of a small amount of carbon, which got further oxidized during the course of the reaction. However, further studies will be needed to clarify these effects in the case of the nanocast catalyst.

Prolonged coke resistance was discussed previously for Ni/La_2O_3 obtained from bulk $LaNiO_3$.[24] However, in these studies, the experiments were performed in pulses, which implies a shorter reaction time to form coke deposits on the catalyst surface compared to that performed over a continuous flow of reactants. Thermogravimetric analysis (TGA) of the catalysts after 48 h of run were performed under oxidizing atmosphere (air) to probe the amount of carbon deposited, as depicted in Figure 9. A slight initial increase in weight was observed for both LN-NCR and LN-CR after the stability tests of 48 h. This weight gain most likely occurs due to (re)oxidation of reduced metallic nickel.[51] No weight loss was observed for LN-NCR confirming the absence of carbon on this catalyst after prolonged exposure to the reactant stream. In contrast, for LN-CR, a large weight loss step approximately between 300 and 500 °C was observed, indicating the presence of amorphous carbon, followed by a much smaller one above 600 °C indicating the burning of more graphitic-like carbon. Together, these two steps account for 20% of carbon deposited during the dry reforming reaction on LN-CR. Furthermore, evidence for carbon deposition can also be obtained from the Raman spectra of the used catalysts after the 48 h run. As viewed from Figure 9 (inset), the Raman spectrum of LN-CR shows two bands: the disorder induced band (D band) centered around 1370 cm^{-1} and the graphitic band (G band) centered around 1593 cm^{-1}. The first one indicates the presence of defective polycrystalline carbonaceous materials, and the second peak indicated the presence of carbonaceous materials that are of graphitic nature. Differently, for LN-NCR, no noticeable peaks were observed in this region, which confirmed the absence of carbon formation for this nanocast catalyst.

From the above results, it thus appears that the H_2/CO ratio increases during reaction over LN-CR because carbon species are formed and deposited on the catalyst. The formation of this byproduct leads to the decrease in the CO production in favor of the production of H_2, which is reflected in the increase in the H_2/CO ratio.[51,52] Such a change in the selectivity is not observed for the nanocast Ni/La_2O_3, where the H_2/CO ratio remains close to unity over 48 h of reaction, as no coke formation is observed.

Moreover, wide-angle XRD analysis of the spent catalysts after 48 h of run reveal reflections corresponding to $La_2O_2CO_3$, Ni^0, $La(OH)_3$, and some comparatively low intensity peaks corresponding to rare earth silicates in the case of the catalyst derived from nanocast $LaNiO_3$, as shown in Figure 10. Because the size of Ni^0 particles is one of the most important parameters that controls the coke formation on the surface,[23,53] we compared the particle sizes of the used catalysts with the fresh ones. For LN-CR, prolonged exposure to the reactant stream resulted in the sintering of Ni^0 particles leading to marked size enhancement which in turn facilitated coke formation. In the case of LN-NCR under the same testing conditions, the Ni^0

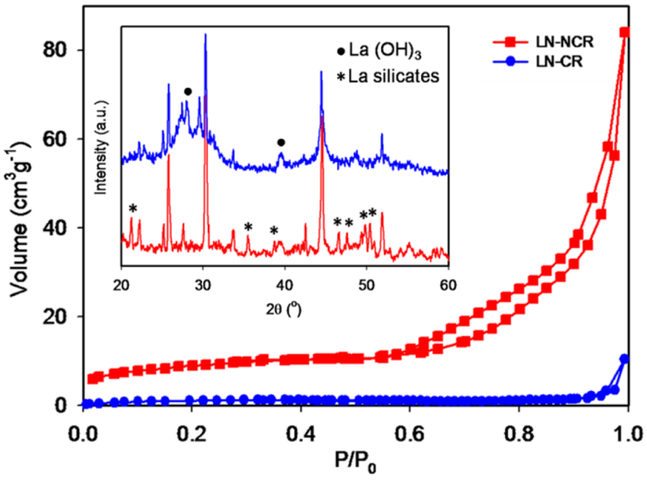

Figure 10. N_2 physisorption isotherms and wide-angle XRD patterns (inset) of Ni/La_2O_3 catalysts obtained from nanocast and bulk $LaNiO_3$ after 48 h on stream at 700 °C.

particle size remained much closer to that observed for the fresh catalyst. Also, for the used catalysts, a decrease in BET surface area was observed for both the materials derived from the bulk and the nanocast perovskites (see Table 3).

Table 3. Structural Parameters Obtained for Ni/La_2O_3 Catalysts after Performing Stability Tests

sample	S_{BET}[a] (m^2g^{-1})	D_p[b] (nm)	Vp[c] (cm^3g^{-1})	Ni_{XRD}[d] (nm)
LN-CR	3	-	-	47
LN-NCR	30	8.1	0.1	16

[a] Specific BET surface area. [b] NLDFT average pore size. [c] Total pore volume. [d] Ni particle size calculated by the Scherrer method.

The observed formation of rare earth silicates is resulting from interactions with residual parts of the SiO_2 template (SBA-15), which cannot be completely removed during the leaching step with NaOH.[54,55] Because we did not observe the presence of rare earth silicates in the XRD patterns of as-synthesized or reduced perovskites, it is clear that these silicates remained amorphous and were crystallized over the long-term exposure to the reactant gases.[54] This suggests that the contribution of these residual silicates toward the surface area of the nanocast $LaNiO_3$ is almost negligible because a decline in specific surface area was observed after reduction at 700 °C. Also, because no reflections corresponding to nickel silicates were observed in the wide-angle region of XRD, it is clear that the active phase remained unaffected.

The coke resistance of Ni/La_2O_3 is generally attributed to the presence of $La_2O_2CO_3$.[21−24] Because we clearly observed the presence of $La_2O_2CO_3$ in the XRD patterns, it is obvious that a similar effect is taking place in the case of the nanocast catalyst as well. Another important phenomenon responsible for the enhanced conversion efficiency and high stability of the nanocast catalyst is the confinement effect occurring owing to the mesoporous architecture. The reduction treatment of the mesoporous perovskite resulted in the formation of Ni^0 particles well-dispersed on the La_2O_3 matrix, which thus played an important role in controlling particle growth. In the perosvkite structure, Ni^{3+} cations are atomically dispersed in each unit cell. Upon reduction, the perovskite structure is progressively destroyed and Ni nanoparticles form, being supported on a La_2O_3 matrix. However, because the entire framework is initially a perovskite structure, Ni should be uniformly distributed through the walls and surfaces. It is likely that, under these conditions, small Ni particles could be less mobile and therefore less prone to sintering (their diffusion being restricted by the La_2O_3 framework). In addition, a contribution of the small amount of silicon-based species, which are remaining in the composition after NaOH treatment, cannot be excluded. These silicate species could also increase the stability of the nanoparticles by limiting their mobility. Such effects would be in line with previous reports describing the stabilizing role of an oxide framework in interaction with the metallic Ni particles.[51,56−58]

The LN-NCR sample is believed to be more coke-resistant because of the higher dispersion of the small Ni species, with a restricted mobility, being “trapped” in an oxide framework, thus avoiding sintering. It is well-documented that smaller Ni particles showed improved coke resistance, due to their enhanced reactivity. However, as discussed for other related systems,[51,56−60] the presence of a higher fraction of metal-oxide boundary in the nanostructured material could also help to keep balance between the rates of CH_4 decomposition and CO_2 dissociation, thus contributing to the improved stability. Sufficiently strong interactions between the metal and the support are believed to be the key to resist sintering (or promote dispersion) and reduce the deposition of carbon on the reduced catalyst. Additionally, it cannot be excluded that the crystallization of rare earth silicate species during the reaction could also contribute in controlling the sintering of the particles.

4. CONCLUSIONS

To conclude, we have synthesized high surface area mesoporous $LaNiO_3$ by the nanocasting method, and the structural and phase changes occurring upon exposure of the material to a reducing environment at high temperature (700 °C) were studied. The catalyst obtained from nanocast $LaNiO_3$ was found to be highly promising toward applications in the dry reforming process. Much higher conversions and enhanced stability toward coke formation were observed for mesoporous Ni/La_2O_3 in comparison to similar compositions synthesized by the conventional process. In the case of the nanocast-derived catalyst, the mesoporous architecture, high surface area, higher pore volume, and large pore size could supply more catalytically active Ni^0 sites accessible to the reactants, and hence superior conversions for both of the reactants. Most critically, no coke formation was observed for the mesoporous catalyst under the present conditions, which in turn reflects a substantially enhanced stability of the nanocast catalyst. Although negligible interference with impurity silicate phases (produced over long-term operation, e.g., 48 h) was observed on the efficiency of the nanocast catalyst, further studies are in progress to elucidate the role of these silicates on the surface properties of the catalysts. In addition, in order to establish the technical feasibility, other process conditions and long-term stability over hundreds of hours should also be verified. Such studies are ongoing in our laboratories and will be reported in a later study.

■ ASSOCIATED CONTENT

Ⓢ Supporting Information

N_2 physisorption isotherm and the corresponding pore size distribution of ordered mesoporous silica SBA-15 aged at 100 °C, Ni (3p) XPS spectra of nanocast $LaNiO_3$ and Ni/La_2O_3

catalysts obtained from nanocast $LaNiO_3$, temperature-dependent variation of experimental product ratios obtained for methane dry reforming over nanocast and bulk $LaNiO_3$ perovskites. This material is available free of charge via the Internet at http://pubs.acs.org.

AUTHOR INFORMATION

Corresponding Authors

*E-mail: freddy.kleitz@chm.ulaval.ca. Fax: (+1) 418 656 7916.
*E-mail: serge.kaliaguine@gch.ulaval.ca. Fax: (+1) 418 656 3810.

Notes

The authors declare no competing financial interest.

ACKNOWLEDGMENTS

The authors acknowledge the financial support from the National Science and Engineering Research Council (Canada) and the Fonds québécois de la recherche sur la nature et les technologies (FRQNT). We thank Dr. Y. Seo and Prof. R. Ryoo (KAIST, Daejeon, Republic of Korea) for providing the high-resolution SEM images of the nanocast $LaNiO_3$ sample.

REFERENCES

(1) Besenbache, F.; Chorkendorf, I.; Clausen, B. S.; Hammer, B.; Molenbroek, A. M.; Norskov, J. K.; Stensgaard, I. *Science* **1998**, *279*, 1913−1915.
(2) Tada, M.; Zhang, S.; Malwadkar, S.; Ishiguro, N.; Soga, J.; Nagai, Y.; Tezuka, K.; Imoto, H.; Otsuka, S.; Ohkoshi, S.; Iwasawa, Y. *Angew. Chem., Int. Ed.* **2012**, *51*, 9361−9365.
(3) Wu, X.; Kawi, S. *Energy Environ. Sci.* **2010**, *3*, 334−342.
(4) Sun, N.; Wen, X.; Wang, F.; Wei, W.; Sun, Y. *Energy Environ. Sci.* **2010**, *3*, 366−369.
(5) Wang, S.; Lu, G. Q. *Energy Fuels* **1998**, *12*, 248−256.
(6) Baudouin, D.; Szeto, K. C.; Laurent, P.; De Mallmann, A.; Fenet, B.; Veyre, L.; Rodemerck, U.; Coperet, C.; Thieuleux, C. *J. Am. Chem. Soc.* **2012**, *134*, 20624−20627.
(7) Burch, R.; Petch, M. I. *Appl. Catal.* **1992**, *88*, 39−60.
(8) Bradford, M. C. J.; Vannice, M. A. *Catal. Rev. Sci. Eng.* **1999**, *41*, 1−42.
(9) Wang, S.; Lu, G. Q. *Energy Fuels* **1996**, *10*, 896−904.
(10) Liu, D.; Lau, R.; Borgna, A.; Yang, Y. *Appl. Catal., A* **2009**, *358*, 110−118.
(11) Souza, M. M. V. M; Aranda, D. A. G.; Schmal, M. *J. Catal.* **2001**, *204*, 498−511.
(12) Bengaard, H. S.; Norskov, J. K.; Sehested, J. S.; Clausen, B. S.; Nielsen, L. P.; Molenbrock, A. M.; Rostrup-Nielsen, J. R. *J. Catal.* **2002**, *209*, 365−384.
(13) Garcia-Dieguez, M.; Pieta, I. S.; Herrera, M. C.; Larubia, M. A.; Alemany, L. J. *J. Catal.* **2010**, *270*, 136−145.
(14) Peters, A.; Nouroozi, F.; Richter, D.; Lutecki, M.; Glaser, R. *ChemCatChem* **2012**, *3*, 598−606.
(15) Pompeo, F.; Nichio, N. N.; Gonzalez, M. G.; Montes, M. *Catal. Today* **2005**, *107*, 856−862.
(16) Djaidja, A.; Libs, S.; Kiennemann, A.; Barama, A. *Catal. Today* **2006**, *113*, 194−200.
(17) Xu, L.; Song, H.; Chou, L. *ACS Catal.* **2012**, *2*, 1331−1342.
(18) Fan, M.; Abdullah, A. Z.; Bhatia, S. *ChemSusChem* **2011**, *4*, 1643−1653.
(19) Liu, C.; Ye, J.; Jiang, J.; Pan, Y. *ChemCatChem* **2011**, *3*, 529−541.
(20) Rebeiro, N. F. P.; Neto, R. C. R.; Moya, S. F.; Souza, M. M. V. M; Schmal, M. *Int. J. Hydrogen Energy* **2010**, *35*, 11725−11732.
(21) Rivaz, I.; Alvarez, J.; Pietri, E.; Perez-Zurita, M. J.; Goldwasser, M. R. *Catal. Today* **2010**, *149*, 388−393.
(22) Valderrama, G.; Goldwasser, M. R.; de Navarro, C. U.; Tatibouet, J. M.; Barrault, J.; Batiot-Dupeyrat, C.; Martinez, F. *Catal. Today* **2005**, *107*, 785−791.
(23) Rivas, M. E.; Fierro, J. L. G.; Goldwasser, M. R.; Pietri, E.; Perez-Zurita, M. J.; Griboval-Constant, A.; Leclercq, G. *Appl. Catal., A* **2008**, *344*, 10−19.
(24) Gallego, G. S.; Mondragon, F.; Barrault, J.; Tatibouet, J. M.; Batiot-Dupeyrat, C. *Appl. Catal., A* **2006**, *311*, 164−171.
(25) Pereneguez, R.; Gonzalaz-de la Cruz, V. M.; Caballero, A.; Holgado, J. P. *Appl. Catal., B* **2012**, *123*, 324−332.
(26) Lu, A. H.; Schüth, F. *Adv. Mater.* **2006**, *18*, 1793−1805.
(27) Tiemann, M. *Chem. Mater.* **2008**, *20*, 961−971.
(28) Yen, H.; Seo, Y.; Kaliaguine, S.; Kleitz, F. *Angew. Chem., Int. Ed.* **2012**, *51*, 12032−12035.
(29) Jiao, F.; Harrison, A.; Hill, A. H.; Bruce, P. G. *Adv. Mater.* **2007**, *19*, 4063−4066.
(30) Tiemann, M. *Chem.—Eur. J.* **2007**, *13*, 8376−8388.
(31) Nair, M. M.; Kleitz, F.; Kaliaguine, S. *ChemCatChem* **2012**, *4*, 387−394.
(32) Jiao, F.; Shaju, K. M.; Bruce, P. G. *Angew. Chem., Int. Ed.* **2005**, *44*, 6550−6553.
(33) Choi, M.; Heo, W.; Kleitz, F.; Ryoo, R. *Chem. Commun.* **2003**, 1340−1341.
(34) Kleitz, F.; Bérubé, F.; Guillet-Nicolas, R.; Yang, C. M.; Thommes, M. *J. Phys. Chem. C* **2010**, *114*, 9344−9355.
(35) Ravikovitch, P. I.; Neimark, A. V. *J. Phys. Chem. B* **2001**, *105*, 6817−6823.
(36) Rumplecker, A.; Kleitz, F.; Salabas, E.; Schüth, F. *Chem. Mater.* **2007**, *19*, 485−496.
(37) de Lima, S. M.; Assaf, J. M. *Catal. Lett.* **2006**, *108*, 63−70.
(38) Kuras, M.; Roucou, R.; Petit, C. *J. Mol. Catal. A* **2007**, *265*, 209−217.
(39) Echchahed, B.; Kaliaguine, S.; Alamdari, H. *Int. J. Chem. React. Eng.* **2006**, *4*, A29.
(40) Kapokova, L.; Pavlova, S.; Bunina, R.; Alikina, G.; Krieger, T.; Ishchenko, A.; Rogov, V.; Sadykov, V. *Catal. Today* **2011**, *164*, 227−233.
(41) Xu, L.; Song, H.; Chou, L. *ACS Catal.* **2012**, *2*, 1331−1342.
(42) Nikoo, M. K.; Amin, N. A. S. *Fuel. Process. Technol.* **2011**, *92*, 678−691.
(43) Alberton, A. L.; Souza, M. M. V. M; Schmal, M. *Catal. Today* **2007**, *123*, 257−264.
(44) Galuzka, J.; Pandey, R. N.; Ahmed, S. *Catal. Today* **1998**, *46*, 83−89.
(45) Adesina, A. A. *Curr. Opin. Chem. Eng.* **2012**, *1*, 272−280.
(46) Ginsburg, J. M.; Pina, J.; Solh, T. E.; de Lasa, H. I. *Ind. Eng. Chem. Res.* **2005**, *44*, 4846−4854.
(47) Batiot-Dupeyrat, C.; Valderrama, G.; Meneses, A.; Martinez, F.; Barrault, J.; Tatibouet, J. M. *Appl. Catal., A* **2003**, *248*, 143−151.
(48) de Sousa, F. F.; de Sousa, H. S. A.; Oliveira, A. C.; Junior, M. C. C.; Ayala, A. P.; Barros, E. B.; Viana, B. C.; Filho, J. M.; Oliveira, A. C. *Int. J. Hydrogen Energy* **2012**, *37*, 3201−3212.
(49) Liu, D.; Quek, X. Y.; Cheo, W. N. E.; Lau, R.; Borgna, A.; Yang, Y. *J. Catal.* **2009**, *266*, 380−390.
(50) Daza, C. E.; Gallego, J.; Moreno, J. A.; Mondragon, F.; Moreno, S.; Molina, R. *Catal. Today* **2008**, *133*, 357−366.
(51) Wang, N.; Yu, X.; Wang, Y.; Chu, W.; Liu, M. *Catal. Today* **2013**, *212*, 98−107.
(52) Li, Y.; Wang, Y.; Zhang, X.; Mi, Z. *Int. J. Hydrogen Energy* **2008**, *33*, 2507−2514.
(53) Hu, Y. H. *Catal. Today* **2009**, *148*, 206−211.
(54) Sarshar, Z.; Kleitz, F.; Kaliaguine, S. *Energy Environ. Sci.* **2011**, *4*, 4258−4269.
(55) Bernal, S.; Blanco, G.; Calvino, J. J.; Cauqui, M. A.; Rodriguez-Isquierdo, J. M.; Vidal, H. *J. Alloys Comp.* **1994**, *250*, 461−466.
(56) Zhang, Q. H.; Li, Y.; Xu, B. Q. *Catal. Today* **2004**, *98*, 601−605.
(57) Xu, B. Q.; Wei, J. M.; Yu, Y. T.; Li, Y.; Li, J. L.; Zhu, Q. M. *J. Phys. Chem. B* **2003**, *107*, 5203−5207.

(58) Hou, Z.; Gao, J.; Guo, J.; Liang, D.; Lou, H.; Zheng, X. *J. Catal.* **2007**, *250*, 331−341.
(59) Hu, Y. H.; Ruckenstein, E. *Catal. Rev. Sci. Eng.* **2002**, *44*, 423−453.
(60) Wang, Y. H.; Liu, H. M.; Xu, B. Q. *J. Mol. Catal.* **2009**, *299*, 44−52.